



HAL
open science

Stabilization of the Trigonal Langasite Structure in $\text{Ca}_3\text{Ga}_{2-2x}\text{Zn}_x\text{Ge}_{4+x}\text{O}_{14}$ ($0 < X < 1$) with Partial Ordering of Three Isoelectronic Cations Characterized by a Multitechnique Approach

Haytem Bazzaoui, Cécile Genevois, Dominique Massiot, Vincent Sarou-kanian, Emmanuel Veron, Sébastien Chenu, Přemysl Beran, Michael J Pitcher, Mathieu Allix

► To cite this version:

Haytem Bazzaoui, Cécile Genevois, Dominique Massiot, Vincent Sarou-kanian, Emmanuel Veron, et al.. Stabilization of the Trigonal Langasite Structure in $\text{Ca}_3\text{Ga}_{2-2x}\text{Zn}_x\text{Ge}_{4+x}\text{O}_{14}$ ($0 < X < 1$) with Partial Ordering of Three Isoelectronic Cations Characterized by a Multitechnique Approach. *Inorganic Chemistry*, 2022, 61 (24), pp.9339-9351. 10.1021/acs.inorgchem.2c01173 . hal-03715396

HAL Id: hal-03715396

<https://hal.science/hal-03715396>

Submitted on 4 Oct 2022

HAL is a multi-disciplinary open access archive for the deposit and dissemination of scientific research documents, whether they are published or not. The documents may come from teaching and research institutions in France or abroad, or from public or private research centers.

L'archive ouverte pluridisciplinaire **HAL**, est destinée au dépôt et à la diffusion de documents scientifiques de niveau recherche, publiés ou non, émanant des établissements d'enseignement et de recherche français ou étrangers, des laboratoires publics ou privés.

Stabilization of the trigonal langasite structure in $\text{Ca}_3\text{Ga}_{2-2x}\text{Zn}_x\text{Ge}_{4+x}\text{O}_{14}$ ($0 \leq x \leq 1$) with partial ordering of three isoelectronic cations characterized by a multi-technique approach

Haytem Bazzouai^a, Cécile Genevois^a, Dominique Massiot^a, Vincent Sarou-Kanian^a, Emmanuel Veron^a, Sébastien Chenu^b, Přemysl Beran^{c,d}, Michael J. Pitcher^{a*} and Mathieu Allix^{a*}

^a CEMHTI, CNRS UPR 3079, 1d Avenue de la Recherche Scientifique, 45071 Orléans, France.

^b Rennes Institute of Chemical Sciences, UMR CNRS 6226, Beaulieu Campus, 263 Av. Général Leclerc, 35042 Rennes, France

^c Nuclear Physics Institute of the CAS, Hlavní 130, 250 68 Řež, Czech Republic

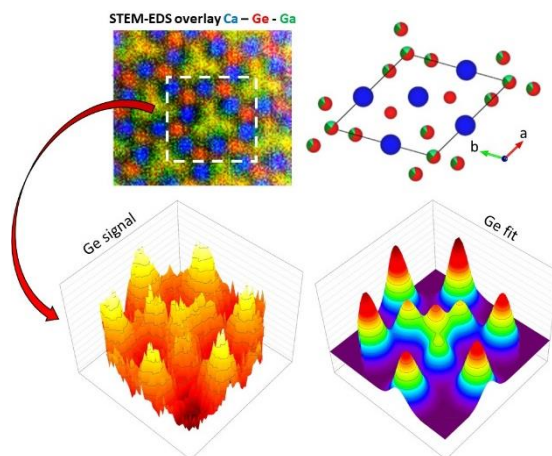
^d European Spallation Source, ESS ERIC, Box 176, SE-22100 Lund, Sweden

E-mail: mathieu.allix@cnrs-orleans.fr michael.pitcher@cnrs-orleans.fr

KEYWORDS: Langasite solid solution, full glass crystallization, out of equilibrium, 2D STEM-EDS fit.

Abstract

Crystallization of oxide glasses rich in Zn^{2+} , Ga^{3+} and Ge^{4+} is of interest for the synthesis of new transparent ceramics. In this context, we report the identification and detailed structural characterization of a new solid solution $\text{Ca}_3\text{Ga}_{2-2x}\text{Zn}_x\text{Ge}_{4+x}\text{O}_{14}$ ($0 \leq x \leq 1$). These compounds adopt the trigonal langasite structure type, offering three possible crystallographic sites for the coordination of isoelectronic Zn^{2+} , Ga^{3+} and Ge^{4+} . We used neutron diffraction to determine distributions of $\text{Ga}^{3+}/\text{Ge}^{4+}$ and $\text{Zn}^{2+}/\text{Ge}^{4+}$ in the simpler end-members $\text{Ca}_3\text{Ga}_2\text{Ge}_4\text{O}_{14}$ and $\text{Ca}_3\text{ZnGe}_5\text{O}_{14}$, whilst for the complex intermediate member $\text{Ca}_3\text{GaZn}_{0.5}\text{Ge}_{4.5}\text{O}_{14}$ we used an original approach combining quantitative 2D analysis of atomic-resolution STEM-EDS maps with neutron diffraction. This revealed that, across the solid solution, the tetrahedral D-sites remain fully occupied by Ge^{4+} , whilst Zn^{2+} , Ga^{3+} and the remaining Ge^{4+} are shared between octahedral B- and tetrahedral C-sites in proportions that depend upon their relative ionic radii. The adoption of the trigonal langasite structure by glass-crystallized $\text{Ca}_3\text{ZnGe}_5\text{O}_{14}$, a compound which was previously observed only in a distorted monoclinic langasite polymorph, is attributed to substantial disorder between Zn^{2+} and Ge^{4+} over the B and C sites. The quantitative 2D refinement of atomic resolution STEM-EDS maps is applicable to a wide range of materials where multiple cations with poor scattering contrast are distributed over different crystallographic sites in a crystal structure.



1. Introduction

Controlled crystallization of glass precursors in ternary or quaternary phase fields is a demonstrated route to technologically useful transparent ceramics by offering suitable control of the microstructure to minimize light scattering.¹⁻⁸ We previously reported long lasting red luminescence in the spinel $\text{Zn}_{1+x}\text{Ga}_{2-2x}\text{Ge}_x\text{O}_4:\text{Cr}^{3+}$,⁹ followed by the synthesis of transparent glass-ceramics at similar compositions by controlled crystallization of $\text{Na}_2\text{O} - \text{ZnO} - \text{Ga}_2\text{O}_3 - \text{GeO}_2$ glass precursors. In these materials, Zn^{2+} , Ga^{3+} and Ge^{4+} undergo a nanoscale phase segregation to leave a dispersion of ZnGa_2O_4 nanocrystals embedded in a GeO_2 -rich glassy matrix,¹⁰ producing bulk glass-ceramics with high transparency in the visible and infra-red spectral regions. Such materials can be functionalized by the addition of Cr^{3+}

to induce long-lasting red luminescence in the full volume of the ceramic.¹¹ Other multinary oxide phase fields containing Zn, Ga and Ge are therefore of interest for their potential to host controllable phase separation phenomena and hence optically transparent functionalizable glass ceramics. The existence in the phase diagram of a stable high-symmetry crystal structure able to host multiple cations, thus fulfilling the role of ZnGa_2O_4 , may be an advantage in this respect. Solid solutions of the langasite-type compounds $\text{Ca}_3\text{Ga}_2\text{Ge}_4\text{O}_{14}$ and $\text{Ca}_3\text{ZnGe}_5\text{O}_{14}$ are therefore of interest as potential nano-crystallization products from $\text{CaO} - \text{ZnO} - \text{Ga}_2\text{O}_3 - \text{GeO}_2$ precursor glasses.

The langasite structure, of general formula $\text{A}_3\text{BC}_3\text{D}_2\text{O}_{14}$, is a layered framework structure type

constructed from corner-sharing (C,D)O₄ tetrahedra and BO₆ octahedra; the BO₆ octahedra also bridge adjacent layers, forming 8-coordinate inter-layer sites for A cations, which are arranged in channels along the stacking axis (Figure 1). The structure type, which is of interest for properties arising from its polarity,^{5,6,12} optical transparency^{3,4} or ability to host interstitial oxide ions,¹³ can accommodate multiple cations with different coordination preferences: the A sites tend to host alkaline- and rare-earth cations, whilst transition metal and *p*-block cations tend to be distributed across the corner-linked B, C and D sites. Ca₃Ga₂Ge₄O₁₄ is readily synthesized in bulk and adopts the common trigonal langasite structure (space group *P321*). In contrast, Ca₃ZnGe₅O₁₄ appears to be difficult to synthesize in bulk, and has only been isolated in the form of small single crystals as a by-product from the synthesis of CaCu_{0.95}Zn_{0.05}Ge₂O₆;¹⁴ it adopts a distorted langasite framework, corresponding to a two-fold expansion of the parent unit cell and reducing the symmetry from *P321* to its monoclinic subgroup *C2* (a distortion that is also observed in certain temperature and pressure regimes for other langasites such as La₃Nb_{0.5}Ga_{5.5}O₁₄).^{15,16} The trigonal and monoclinic unit cells are projected together onto the same underlying langasite structure in Figure 1.

In both compounds, the absence of X-ray scattering contrast between Ga³⁺/Ge⁴⁺ and Zn²⁺/Ge⁴⁺ means that the distribution of these cations over the three framework sites (B, C and D) cannot be obtained directly by conventional (non-anomalous) X-ray diffraction methods, and instead indirect routes (e.g. analysis based on refined bond distances) have been used to deduce the nature and extent of cation ordering.¹⁷ Such isoelectronic pairs can be distinguished directly by neutron diffraction (NPD), as demonstrated for La₃Ga_{5-x}Ge_{1+x}O_{14+x/2},¹³ but NPD alone cannot be used for direct analysis of more complex systems with three or more isoelectronic cations distributed over the framework sites B, C and D. Atomic resolution STEM-EDS mapping offers a solution to this problem by detecting each element type directly with a spatial resolution of around 2-3 Å. Whilst this technique is most often used qualitatively, intensities of atomic columns can be extracted by Gaussian curve fitting which is most often applied to 1D line profiles to provide quantitative information about atomic site occupancies.¹⁸ Furthermore, Gaussian fitting of entire 2D map sections has been demonstrated for SrTiO₃ thin films,¹⁹ and then applied to distinguish multiple elements with close atomic number in FeCoNi alloys²⁰. The 2D fitting approach has the advantage of considering the actual nature of the two-dimensional dataset: it reduces errors associated with the subjective selection of the location and boundaries of a line profile (which is problematic where the atomic columns of interest do not lie on a perfectly straight line, or where adjacent columns overlap to contribute unwanted

intensity to the profile), and produces contour maps that are more intuitive for crystallographic problems.

It can be challenging to characterize cation ordering in crystalline systems where the scatterers have a similar atomic number, or where there are more than two cation species involved in the ordering, especially when the ordering is incomplete. The ability to resolve such problems is important in many contexts, for example where cation ordering controls structural polarity,²¹ suppresses thermal conductivity,²² or influences lithium battery cyclability.²³ Here, we report the synthesis of a complete solid solution (1-x)Ca₃Ga₂Ge₄O₁₄ – (x)Ca₃ZnGe₅O₁₄ (0 ≤ x ≤ 1) by full crystallization from glass, with full structural characterization by synchrotron PXRD and neutron diffraction, and quantitative use of atomic resolution STEM-EDS on powder specimens based on the development of a 2D fitting procedure to extract quantitative information on the distribution of Zn²⁺, Ga³⁺ and Ge⁴⁺ over the available framework sites in the x = 0.5 member Ca₃Zn_{0.5}GaGe_{4.5}O₁₄.

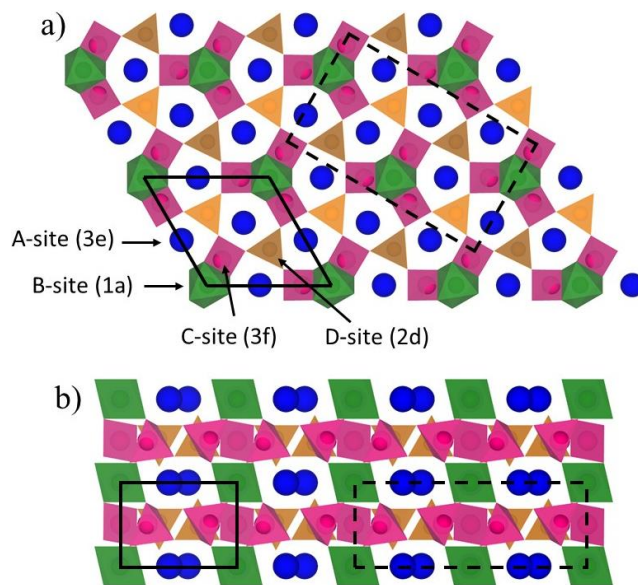


Figure 1. Crystal structure projection of the A₃BC₃D₂O₁₄ langasite structure family along the a) *c*-axis, b) *b*-axis, showing both the *P321* cell (straight black lines) and *C2* cell (dashed black lines).

2. Experimental

2.1. Synthesis Procedure.

Samples of composition Ca₃Ga_{2-2x}Zn_xGe_{4+x}O₁₄ were synthesized either by direct crystallization of the melt (for x = 0), or by full and congruent crystallization from glass (for 0.25 ≤ x ≤ 1). First, stoichiometric amounts from high purity precursors CaCO₃ 99.95%, Ga₂O₃ 99.998%, ZnO 99.999%, GeO₂ 99.9% (all from Strem Chemicals) were weighed according to the nominal composition for 0 < x ≤ 1. For x=0, an excess of 2% (wt%) of GeO₂ was added to the initial mixture to compensate for partial volatilization (see Figure S1). The precursors were then ground together for several

minutes in an agate mortar using ethanol to improve the homogeneity of the mixture. The resulting powder was dried and pressed into pellets, then divided into fragments of ~35 mg each. Pellet chunks were melted individually by aerodynamic levitation (ADL) in an argon gas jet coupled to two CO₂ lasers (10.6 μm). These samples melted between 1250°C – 1350°C (depending on the composition), and were further heated up to 1500°C to ensure their homogeneity, then subsequently quenched by turning the lasers off, reaching high cooling rates (estimated around 300°C/s) in order to achieve vitrification, and leading to glass precursors in the form of spherical beads for Ca₃Ga_{2-2x}Zn_xGe_{4+x}O₁₄ with compositions 0.25 ≤ x ≤ 1. For Ca₃Ga₂Ge₄O₁₄ (x=0), the argon gas flow was adjusted so that the levitating molten bead touches the nozzle. The contact surface thus acts as a nucleation centre for crystallization of the entire bead when the lasers are turned off. This process produced a higher crystallinity of the sample compared to glass crystallized samples of the composition, as confirmed by laboratory PXRD, showing narrower diffraction peaks for the molten liquid crystallized sample compared to the glass crystallized sample (see Figure S3). The amorphous (0.25 ≤ x ≤ 1)/crystalline (x=0) state of resulting beads was further confirmed by laboratory powder X-ray diffraction (see Figure S2 and S3). The glass precursor samples were then crystallized in air at temperatures between 800°C and 815°C (characteristic crystallization temperatures obtained by DSC, as shown in Figure 2a), for 2-3h (see section 3.1).

2.2. Thermal Analysis.

Differential scanning calorimetry (DSC) was performed on a Setaram MULTI HTC 1600 instrument to determine the glass transition and crystallization temperatures of each composition. A ~300 mg powder sample was used, contained within a platinum crucible, with argon as the purging gas and a heating and cooling rate of 10 °C/min, samples were heated up to 900°C, the measured temperatures have an incertitude of ±2°C.

2.3. Powder Diffraction.

Room temperature laboratory powder X-ray diffraction (PXRD) was performed using a Bruker D8 Advance laboratory diffractometer (Cu K_α radiation) equipped with a LynxEye XE detector in Bragg-Brentano geometry, with powders dispersed on a low-background silicon wafer. *In-situ* variable temperature PXRD was performed using a Bruker D8 Advance laboratory diffractometer (also Cu K_α radiation, Bragg-Brentano geometry) equipped with a Vantec detector and an Anton Paar HTK1200N furnace. Powders obtained from crushed glass beads were placed in a platinum-lined corundum sample holder and heated under air. Data were collected from 30°C to 600°C in one heating step, then to 1200°C using a 10°C step size, an angular range of 20-39° (2θ) with a 0.016° step size and counting time of 0.7 s/step. Synchrotron

powder diffraction (SPD) measurements were collected on the 11BM beamline (Argonne National Laboratory) in the United States, for samples of composition Ca₃Ga_{2-2x}Zn_xGe_{4+x}O₁₄ x=0, 0.25, 0.5, 0.75 and 1. Crystallized beads were crushed to powder (one bead per composition) and filled into 0.8 mm diameter Kapton capillaries. Data were acquired with an incident wavelength of λ=0.458084 Å from 1 to 50° (2θ) with a step size of 0.001° and a 0.1s measuring time per step. Neutron powder diffraction (NPD) data were acquired for samples of composition Ca₃Ga_{2-2x}Zn_xGe_{4+x}O₁₄ x=0, 0.5 and 1, on the instrument MEREDIT at the Nuclear Physics Institute, Czech Republic, with λ=1.46 Å in the range 4-144° (2θ), using a step size of 0.08° and a measuring time of 970 s per step. Samples were scaled up to ~5 g for x=0, 0.5 and ~4 g for x=1, by crushing and combining ~100 individually crystallized beads for neutron diffraction experiments. Structural analysis and Rietveld refinements²⁴ were performed using TOPAS Academic (v.6).²⁵ Bond valence sums (BVS) were calculated by the method of Brown and Altermatt.²⁶

2.4. Transmission Electron Microscopy.

The cation distributions were investigated at the atomic scale via high-resolution Scanning Transmission Electron Microscopy-High Angle Annular Dark Field (STEM-HAADF) imaging and Energy Dispersive X-ray Spectroscopy (EDS) elemental mapping. These experiments were performed on a JEOL ARM200F (JEOL Ltd.) Cold FEG Transmission Electron Microscope (TEM) operating at 200kV, equipped with a double spherical aberration corrector and fitted with a JEOL SDD CENTURIO EDS system. In STEM-HAADF imaging mode, a 68-174.5 mrad inner-outer collection angle and a 0.1nm probe size were used while in STEM-EDS mapping a probe size of 0.13nm was chosen. Fine sample powder was first homogeneously dispersed in ethanol, then one droplet of this suspension was deposited on a TEM amorphous holey carbon-coated copper grid and left to dry.

3. Results

3.1. Synthesis by Crystallization from Glass and Molten-liquid.

Classic solid-state reaction routes were first investigated in the synthesis of Ca₃Ga₂Ge₄O₁₄ (x = 0), however we were not able to prepare single-phase powders by this route (see SI section I for more details). Crystallization from glass was then considered as an alternative synthesis route, as this approach was shown to help accessing new metastable crystalline phases.^{2-4,27} Initial attempts to make precursor glass of composition Ca₃Ga₂Ge₄O₁₄ (x = 0) used a conventional melt-quenching technique, by melting the reaction mixture in a platinum crucible at 1300°C for 1h, then quenching by placing the bottom of the crucible in a

bath of water without any sample-water contact. After thermal treatment, these glasses showed a heterogeneous crystallization leading to a mixture of gallate and germanate phases. In contrast, glass beads produced using the faster cooling rates offered by the ADL apparatus were found to crystallize into single-phase langasite materials after heat treatment at 815°C. By further tuning of the ADL experimental conditions, we found that direct crystallization of the molten bead (see section 2.1) produced single phase langasite materials with sharper diffraction peaks (see Figure S3). We used the directly-crystallized materials for all structural characterizations of the composition $x = 0$.

Single-phase langasite materials were obtained for $0.25 \leq x \leq 1$ by crystallization of precursor glasses obtained by ADL. The highest quality samples were obtained by crystallising the beads in bulk form rather than crushed (powder) form due to surface crystallization of the secondary phases $\text{CaZnGe}_2\text{O}_6$ and $\text{Ca}_2\text{ZnGe}_2\text{O}_7$ (see Figure S4): in-situ PXRD of $\text{Ca}_3\text{ZnGe}_5\text{O}_{14}$ ($x=1$) glass powder shows the crystallization of the langasite phase above 670°C, which occurs simultaneously with crystallization of these minor impurities (Figure 2a). In Figure S5, we show a comparison between DSC heating curves of $\text{Ca}_3\text{ZnGe}_5\text{O}_{14}$ ($x=1$) glass, measured under powder and bulk form. The powder sample exhibits a lower T_c , consistent with a more facile surface crystallization mechanism. As shown in Figure 2b, DSC measurements were conducted on a single glass bead for each composition to determine their glass transition (T_g) and glass crystallization (T_c) temperatures (see Table S1). To achieve full and congruent crystallization from glass, the resulting glass beads for $0 < x < 1$ were heated ~~between their T_g and T_c~~ at 815°C for 2h ($0 < x < 1$) and at 800°C for 3h ($x=1$), under bulk form to prevent surface crystallization of impurities. Beads prepared in this way contained langasite-type $\text{Ca}_3\text{Ga}_{2-2x}\text{Zn}_x\text{Ge}_{4+x}\text{O}_{14}$ as the only crystalline phase.

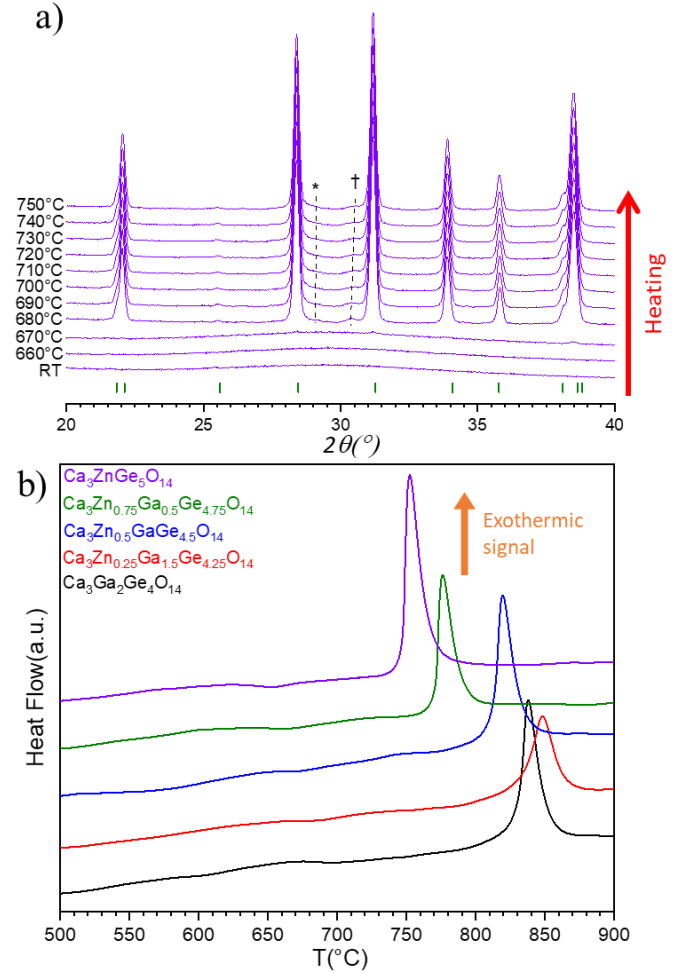


Figure 2. a) Variable temperature PXRD measurements on the $\text{Ca}_3\text{ZnGe}_5\text{O}_{14}$ $x=1$ glass composition showing its crystallization upon heating ($0.5^\circ\text{C}/\text{min}$ heating rates), where * and † represent the $\text{CaZnGe}_2\text{O}_6$ and $\text{Ca}_2\text{ZnGe}_2\text{O}_7$ impurities, respectively. Green tick marks represent the $P321$ $\text{Ca}_3\text{ZnGe}_5\text{O}_{14}$ indexation. b) DSC measurements of $\text{Ca}_3\text{Ga}_{2-2x}\text{Zn}_x\text{Ge}_{4+x}\text{O}_{14}$ $x=0$ (black), 0.25 (red), 0.5 (blue), 0.75 (green) and 1 (purple) samples, using a $10^\circ\text{C}/\text{min}$ rates upon heating.

3.2. Structure evolution from $0 \leq x \leq 1$ by synchrotron XRD

The reported $\text{Ca}_3\text{ZnGe}_5\text{O}_{14}$ monoclinic langasite structure (SG. $C2$, $a=13.938(5)$ Å, $b=7.941(3)$ Å, $c=5.0560(17)$ Å, $\beta=90.817(4)^\circ$),¹⁴ was described as a fully ordered structure where Zn^{2+} cations are accommodated on the octahedral (B) sites, whilst Ge^{4+} cations occupy the remaining tetrahedral (C- and D-) sites. To further investigate the possibility of a monoclinic distortion for glass-crystallized samples close to this composition ($x=1$), SPD measurements were conducted on samples of composition $x=0, 0.25, 0.5, 0.75, 1$.

Across the solid solution, all SPD patterns (Figure S6) could be indexed with the parent hexagonal langasite cell with a systematic peak shift (Figure 3a), and no extra peaks became apparent as the composition approaches $x = 1$, indicating that the $P321$ structure is retained for all compositions. Figure 3b shows a direct comparison between the acquired SPD pattern of

$\text{Ca}_3\text{ZnGe}_5\text{O}_{14}$ ($x=1$), and a simulated SPD pattern of $\text{Ca}_3\text{ZnGe}_5\text{O}_{14}$ (reported $C2$ structure)¹⁴ under the same measuring conditions. The simulated $C2$ diffraction pattern contains many additional Bragg peaks that are not present in the acquired pattern, which is fully indexed to the hexagonal $P321$ $\text{Ca}_3\text{Ga}_2\text{Ge}_4\text{O}_{14}$ cell.

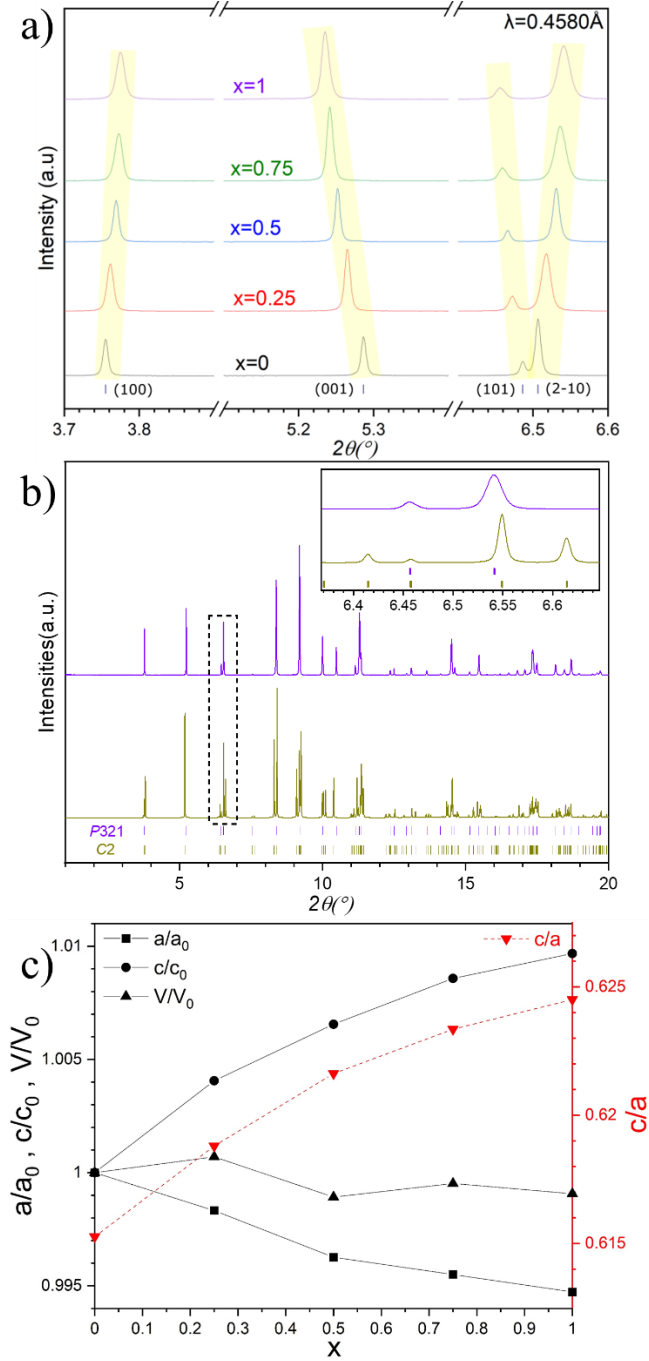


Figure 3. a) Synchrotron powder diffraction data from $\text{Ca}_3\text{Ga}_{2-2x}\text{Zn}_x\text{Ge}_{4+x}\text{O}_{14}$ $x=0$ (black), 0.25 (red), 0.5 (blue), 0.75 (green) and 1 (purple), highlighting the systematic shift of the (100), (001), and (101)/(2 $\bar{1}0$) peaks due to the Ga^{3+} substitution by Zn^{2+} and Ge^{4+} . Dark blue tick marks correspond to $\text{Ca}_3\text{Ga}_2\text{Ge}_4\text{O}_{14}$ (space group $P321$). b) SPD pattern of glass-crystallized $\text{Ca}_3\text{ZnGe}_5\text{O}_{14}$ (purple) compared with a simulated pattern of the previously reported monoclinic $C2$ structure¹⁴ (dark yellow), with their respective cell indexations (dark yellow and purple tick marks). c) Normalized refined cell parameters (from Rietveld analysis) of the $P321$ langasite structure across the

solid solution series to the parent $\text{Ca}_3\text{Ga}_2\text{Ge}_4\text{O}_{14}$ cell parameters.

Rietveld refinements were carried out using the $\text{Ca}_3\text{Ga}_2\text{Ge}_4\text{O}_{14}$ structure reported by Mill *et al.*¹⁷ (SG $P321$, $a = 8.076$ Å, $c = 4.974$ Å) as a starting model for all compositions, keeping the same number of total refined parameters for each sample (15 background terms, zero shift, scale factor, 6 profile parameters (TCHZ profile function), axial divergence and 17 atomic parameters, resulting in 41 refined independent parameters). The B- C- and D-sites were fixed to be fully occupied by cations with no refinement of the Ga^{3+} , Ge^{4+} or Zn^{2+} partial occupancies. The refined cell parameters (from SPD data) show opposing trends in the a and c parameters, giving a very weak decrease in unit cell volume but a marked increase in c/a ratio with increasing x (Figure 3c). Such behaviour is consistent with the substitution of Ga^{3+} (ionic radius of 0.62 and 0.47 Å in 6 and 4-coordination respectively) by a mixture of smaller Ge^{4+} (0.53 and 0.39 Å) and larger Zn^{2+} (0.74 and 0.60 Å),²⁸ and is also seen in other langasite type solid solutions such as $\text{La}_3\text{Ga}_5-x\text{Ge}_{1+x}\text{O}_{14+x/2}$.¹³ The refinements led to satisfactory reliability factors for the entire measured series (see Figures S8 to S10 for SPD Rietveld refinement plots and Tables S2 to S6 for refined structural parameters).

As shown in Figure 3b, the $\text{Ca}_3\text{ZnGe}_5\text{O}_{14}$ ($x = 1$) sample synthesized by glass crystallization produces far fewer Bragg reflections than the previously reported monoclinic ($C2$) structure, and can be indexed fully to the trigonal ($P321$) structure. We also compared the Rietveld fits obtained from both structural models. Provisional refinement of both models produced misfits due to an hkl -dependent peak broadening in the measured pattern. This was modelled using the Stephens description²⁹ for trigonal and monoclinic symmetries respectively, thus reducing the R_{wp} and χ^2 values from [8.98%, 2.01] to [7.36%, 1.35] for the $P321$ model, and from [8.93%, 1.99] to [6.68%, 1.10] for the $C2$ model (see Figures S10, S12 for SPD refinements and Tables S6 to S9 for refined structural parameters). The unit cell of the $C2$ model, refined to an essentially orthorhombic symmetry corresponding to a decrease of β from $90.817(4)^\circ$ (published starting model)¹⁴ to $89.955(1)^\circ$. Even though the $C2$ model provides a marginally better fit to the whole pattern when the Stephens broadening functions are applied, the lower symmetry of this structure allows more refinable parameters (68 + 10 parameters from Stephens description) than the $P321$ space group (41 + 5 parameters from Stephens description), and the refined model is almost indistinguishable from its trigonal counterpart, as shown in Figure S7 an overlay of both refined structures against the same acquired SPD data. We therefore consider the trigonal $P321$ structure to be the simplest and most appropriate description of glass-crystallized $\text{Ca}_3\text{ZnGe}_5\text{O}_{14}$ ($x = 1$).

To test the stability of the $\text{Ca}_3\text{ZnGe}_5\text{O}_{14}$ ($x=1$) $P321$ structure against $T(^{\circ}\text{C})$ and a possible phase transition ($P321 \rightarrow C2$), variable temperature PXRD (VT-PXRD) measurements were carried out on a glass crystallized $\text{Ca}_3\text{ZnGe}_5\text{O}_{14}$ ($x=1$) sample, from room temperature to 700°C in steps of 100°C . As shown on Figure S12, the cell parameters display a linear increasing trend and no discontinuous changes were noticed (as demonstrated in¹⁶ for some langasite compositions under pressure, where their cell parameters trend shows a discontinuity due to a phase transition from $P321$ to $C2$), suggesting that the hexagonal polymorph is retained until its decomposition.

3.3. Distribution of two cations in $x = 0, 1$ end members by neutron diffraction.

The end member compositions ($x = 0, 1$) host only two cation species on the framework (B, C, D) sites, with different neutron scattering lengths (8.185(20) fm,

7.288(2) fm and 5.680(5) fm for Ge, Ga and Zn respectively),³⁰ allowing the use of NPD to refine the Ga/Ge and Zn/Ge ratios directly. Rietveld refinements against NPD data were constrained to keep each mixed site fully occupied and an overall composition matching the nominal, see Figure 4a, Figure 4b for refined plots, and Tables Table 1 and Table 2 for refined structural parameters. The refinements of neutron data for the $x=0$ sample showed that the cationic disorder is distributed over the octahedral 1a and tetrahedral 3f sites (as previously reported in^{17,31}), while the tetrahedral 2d site remains fully occupied by Ge. Refined occupancies led to 0.51(8)Ga/0.49(8)Ge on the 1a site and 0.50(3)Ga/0.50(3)Ge on the 3f site, which displays a complete disorder over these two crystallographic sites (see Table 1 and Table 2). This is consistent with a non-quantitative ^{71}Ga QPASS NMR spectrum collected from the $\text{Ca}_3\text{Ga}_2\text{Ge}_4\text{O}_{14}$ sample, which showed resonances from 6- and 4-coordinate gallium (as described in SI section II).

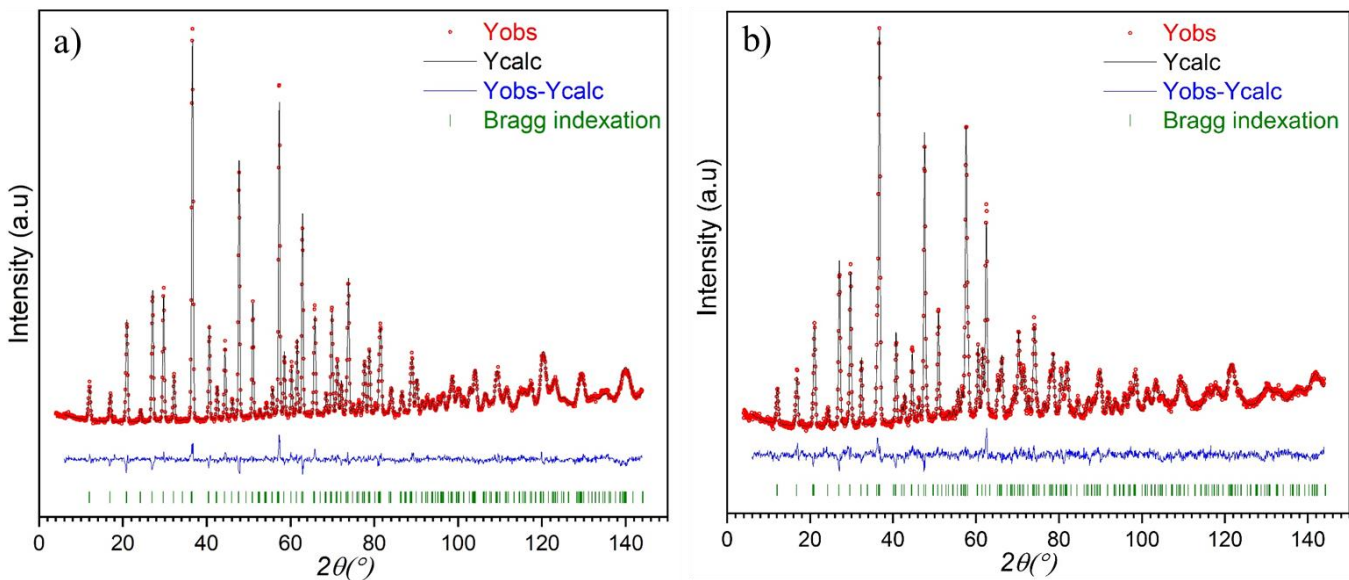


Figure 4. NPD Rietveld refinements plots of a) $\text{Ca}_3\text{Ga}_2\text{Ge}_4\text{O}_{14}$ ($x=0$) $R_p=3.04\%$ $R_{wp}=3.83\%$, b) $\text{Ca}_3\text{ZnGe}_5\text{O}_{14}$ ($x=1$) $R_p=3.43\%$ $R_{wp}=4.35\%$. Observed (red dot), calculated (black line), and difference (blue line) profiles are shown. The green tick marks correspond to allowed reflection positions.

Table 1. Refined structural parameters obtained from NPD data collected at room temperature on $\text{Ca}_3\text{Ga}_2\text{Ge}_4\text{O}_{14}$ ($P321$ space group, $a=8.0712(2)$ Å and $c=4.9680(2)$ Å).

Atom	Position	x	y	z	Occ	Biso
Ca	3e	0.4183(7)	0	0	1	0.91(10)
Ga1/Ge1	1a	0	0	0	0.51(8)/0.49(8)	0.92(5) ^a
Ga2/Ge2	3f	0.7635(4)	0	1/2	0.50(3)/0.50(3)	0.92(5) ^a
Ge3	2d	1/3	2/3	0.5273(9)	1 [*]	0.92(5) ^a
O1	2d	1/3	2/3	0.1843(11)	1	1.18(4) ^b
O2	6g	0.4616(5)	0.3144(4)	0.3113(6)	1	1.18(4) ^b
O3	6g	0.2174(4)	0.0793(4)	0.7667(6)	1	1.18(4) ^b

^{a,b}: constrained to refine to the same Biso values.

^{*}: Fixed at 1 after its initial refined value converged to almost 1.

Table 2. Refined structural parameters obtained from NPD data collected at room temperature on $\text{Ca}_3\text{ZnGe}_5\text{O}_{14}$ ($P321$ space group, $a = 8.0308(3)$ Å and $c = 5.0164(4)$ Å).

Atom	Position	x	y	z	Occ	Biso
Ca	3e	0.4198(8)	0	0	1	1.18(13)
Zn1/Ge1	1a	0	0	0	0.52(4)/0.48(4)	1.09(8) ^a
Zn2/Ge2	3f	0.7674(5)	0	1/2	0.16(1)/0.84(1)	1.09(8) ^a
Ge3	2d	1/3	2/3	0.5295(12)	1 [*]	1.09(8) ^a
O1	2d	1/3	2/3	0.1854(17)	1	2.17(7) ^b
O2	6g	0.4617(7)	0.3173(5)	0.3139(10)	1	2.17(7) ^b
O3	6g	0.2227(6)	0.0785(6)	0.7585(10)	1	2.17(7) ^b

^{a,b}: constrained to refine to the same Biso values.

^{*}: Fixed at 1 after its initial refined value converged to almost 1.

Rietveld refined NPD data for the $x=1$ fully substituted end member also confirmed that the cationic disorder occurs between the 1a and 3f sites, while the 2d site remains fully occupied by Ge atoms. The refined occupancies over the mixed sites, 0.52(4)Zn/0.48(4)Ge on the 1a and 0.16(1)Zn / 0.84(1)Ge on the 3f, show that only Zn atoms are randomly dispersed over the two

coordination types, 52(4)% on the 1a 6-coordinated site and 16(1)% on the 3f 4-coordinated site. The B- and C-site cation-oxide distances show notable differences going from the $\text{Ca}_3\text{Ga}_2\text{Ge}_4\text{O}_{14}$ langasite to the fully Zn/Ge-substituted compound $\text{Ca}_3\text{ZnGe}_5\text{O}_{14}$ (Table 3 and 4).

Table 3. Cation oxide interatomic distances and bond valence sums calculated for all Ga and Ge sites of $\text{Ca}_3\text{Ga}_2\text{Ge}_4\text{O}_{14}$.

Site	Bond	Length (Å)	Site	Bond	Length (Å)	Site	Bond	Length (Å)
B(1a)	<i>M</i> -O3 x6	1.926(3)	C(3f)	<i>M</i> -O3 x2	1.787(4)	D(2d)	<i>M</i> -O1 x1	1.704(7)
				<i>M</i> -O2 x2	1.853(5)		<i>M</i> -O2 x3	1.776(4)
	*BVS (Ga)	3.53(2)		*BVS (Ga)	3.37(2)		*BVS (Ga)	3.72(3)
	*BVS (Ge)	3.71(2)		*BVS (Ge)	3.49(2)		*BVS (Ge)	3.91(3)

*Calculated with a distance cut-off at 3Å

Table 4. Cation oxide interatomic distances and bond valence sums calculated for all Zn and Ge sites of $\text{Ca}_3\text{ZnGe}_5\text{O}_{14}$.

Site	Bond	Length (Å)	Site	Bond	Length (Å)	Site	Bond	Length (Å)
B(1a)	<i>M</i> -O3 x6	1.984(6)	C(3f)	<i>M</i> -O3 x2	1.767(6)	D(2d)	<i>M</i> -O1 x1	1.73(1)
				<i>M</i> -O2 x2	1.862(6)		<i>M</i> -O2 x3	1.770(6)
	*BVS (Zn)	2.74(2)		*BVS (Zn)	3.06(2)		*BVS (Zn)	3.29(3)
	*BVS (Ge)	3.17(2)		*BVS (Ge)	3.58(2)		*BVS (Ge)	3.89(4)

*Calculated with a distance cut-off at 3Å

The B-site *M*-O3 bond length increases from 1.926(3)Å (Ga1/Ge1-O3) to 1.984(6)Å (Zn1/Ge1-O3), which allows an 8.7% increase of the polyhedral volume, whilst both C-site *M*-O3 and *M*-O2 bonds lengths decrease from 1.787(4)Å (Ga2/Ge2-O3) and 1.853(5)Å (Ga2/Ge2-O2), to 1.767(6)Å (Zn2/Ge2-O3) and 1.862(6)Å (Zn2/Ge2-O2) respectively, leading to the 3f site tetrahedron a volume decrease of 2.1%. These results are consistent with the refined occupancies of each site for both end members, where Ga^{3+} is fully exchanged by the larger Zn^{2+} cation on the 1a site, and only 1/3 by the same larger cation on the 3f site, while

the other 2/3 are substituted by a smaller Ge^{4+} cation. The hypothesis of a fully ordered hexagonal langasite structure for both end members was considered by Rietveld refinement with different fixed Ga/Ge and Zn/Ge occupancies on both 1a and 3f sites against NPD data. In Figure S13(a) and S13(b), a shallow χ^2 minimum can be detected when the amount of Ga^{3+} and Zn^{2+} approaches 50% occupancy of the 1a site for $x = 0$ and 1 respectively. Moreover, subtle peak intensity misfits at low angle can be spotted when Ga^{3+} or Zn^{2+} scattering density is focused on one of the two cationic disordered sites, inducing over- or under-calculated

peak intensities (Figure S13(c) and S13(d)). The intensity misfits are more visible for the Zn^{2+} compound $x=1$, compared to the Ga^{3+} compound $x=0$ due to their close neutron scattering lengths.³⁰ Furthermore, bond valence sum (BVS) calculations (Table 3 and Table 4), indicate that only the 2d site is suitable for Ge^{4+} , BVS = 3.91(3) and 3.89(4) with a mean Ge3-O distance of 1.758(4)Å and 1.759(3)Å for both $x=0$ and $x=1$ compounds respectively. For the 1a and 3f sites, the BVS values indicate that all three cations are either under- or over-bonded in the two different coordination types, which is consistent with the partial cation disorder observed by Rietveld refinement. The trend in bond distances and atomic site occupancies from NPD is discussed together with the bond distance trend from SPD across the full series ($x = 0, 0.5, 1$) in Section 4.

3.4. Distribution of three cations in $x = 0.5$ by STEM-EDS and neutron diffraction.

To analyse the distribution of three isoelectronic cations over multiple crystallographic sites, as required for the intermediate composition $\text{Ca}_3\text{GaZn}_{0.5}\text{Ge}_{4.5}\text{O}_{14}$ ($x=0.5$), neutron diffraction must be combined with another complementary technique. Here, our approach is to extract direct quantitative information about the cation distributions by atomic-resolution STEM-EDS, and use this to construct a Rietveld model with appropriate (chemically-justified) constraints on the refined cation occupancies.

In order to visualize the 2D structural projection of the $\text{Ca}_3\text{GaZn}_{0.5}\text{Ge}_{4.5}\text{O}_{14}$, the sample was oriented along the $[001]^*$ direction (Figure 5a) and imaged in STEM-HAADF mode at the atomic scale (Figure 5b, 5c). Along the $[001]^*$ direction, each column of atoms is composed of only one type of crystallographic site with the same density (See Figure 1).

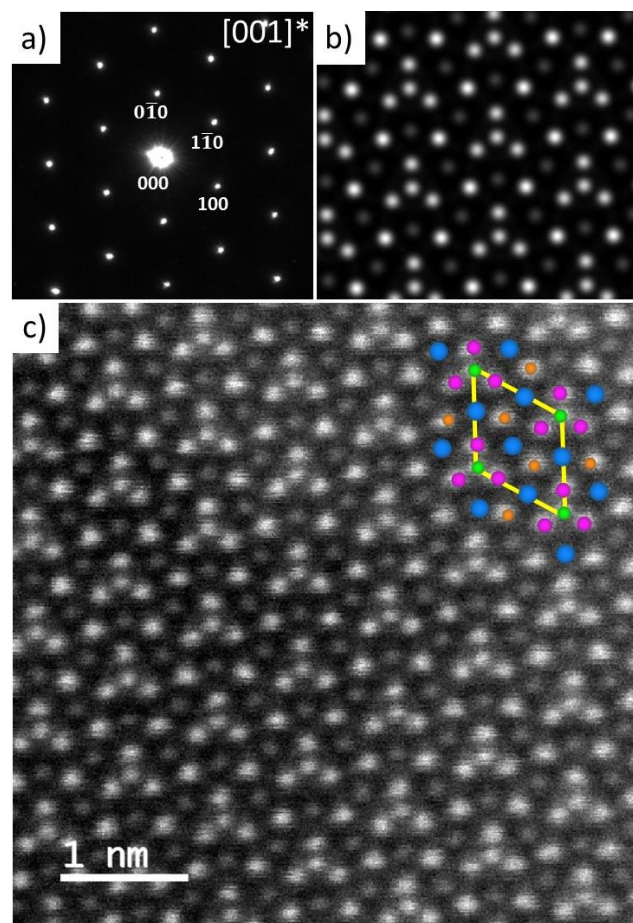


Figure 5. a) Selected area electron diffraction (SAED) pattern of the $\text{Ca}_3\text{GaZn}_{0.5}\text{Ge}_{4.5}\text{O}_{14}$ ($x=0.5$) sample oriented along the $[001]^*$ direction, with b) and c) showing simulated (using JEMS software)³² and measured STEM-HAADF images respectively. The corresponding crystal structure projection is overlaid on the top-right corner of the image, where blue, green, pink and orange points represent the 3e, 1a, 3f and 2d crystallographic sites respectively.

In STEM-HAADF mode, the intensity of the acquired images is proportional to the thickness of the sample (t), the density (ρ) and the average atomic number (Z): $I \propto \rho t Z^n$ with n in the range between 1.6 and 2. The thickness of the sample was measured at 60nm by Electron Energy Loss Spectroscopy (EELS), which represents close to 120 superimposed unit cells (120 atoms per column). It was estimated to remain unchanged across the entire imaged area ($\approx 5 \text{ nm} * 5 \text{ nm}$). In these conditions, the intensity in the STEM-HAADF images is essentially due to the average atomic number (Z) of the crystallographic site. The 3e sites, being composed of the lightest cations ($Z_{\text{Ca}} = 20$), appear the darkest while the 1a, 3f and 2d sites appear brighter due to the presence of heavier cations ($Z_{\text{Ge}} = 32$, $Z_{\text{Ga}} = 31$ and $Z_{\text{Zn}} = 30$). However, as Ge, Ga and Zn are of similar atomic number ($Z_{\text{Ge}} \approx Z_{\text{Ga}} \approx Z_{\text{Zn}}$), it is not possible to determine the distribution of these 3 cations on the 1a, 3f and 2d crystallographic sites using only the intensities of the STEM-HAADF images. Consequently, EDS mapping at the atomic scale was carried out (Figure 6). The maps acquired on several zones of the same grain were aggregated in order to

improve the signal to noise ratio and to tend towards an average model. A Wiener filter was then applied to highlight the atomic positions. The 3e site is clearly visible and composed only of Ca as expected, whilst the

2d site contains only Ge, and the 3f and 1a sites are mixed, which is consistent with the refined structures of $\text{Ca}_3\text{Ga}_{2-2x}\text{Zn}_x\text{Ge}_{4+x}\text{O}_{14}$ both end members $x=0$ and $x=1$.

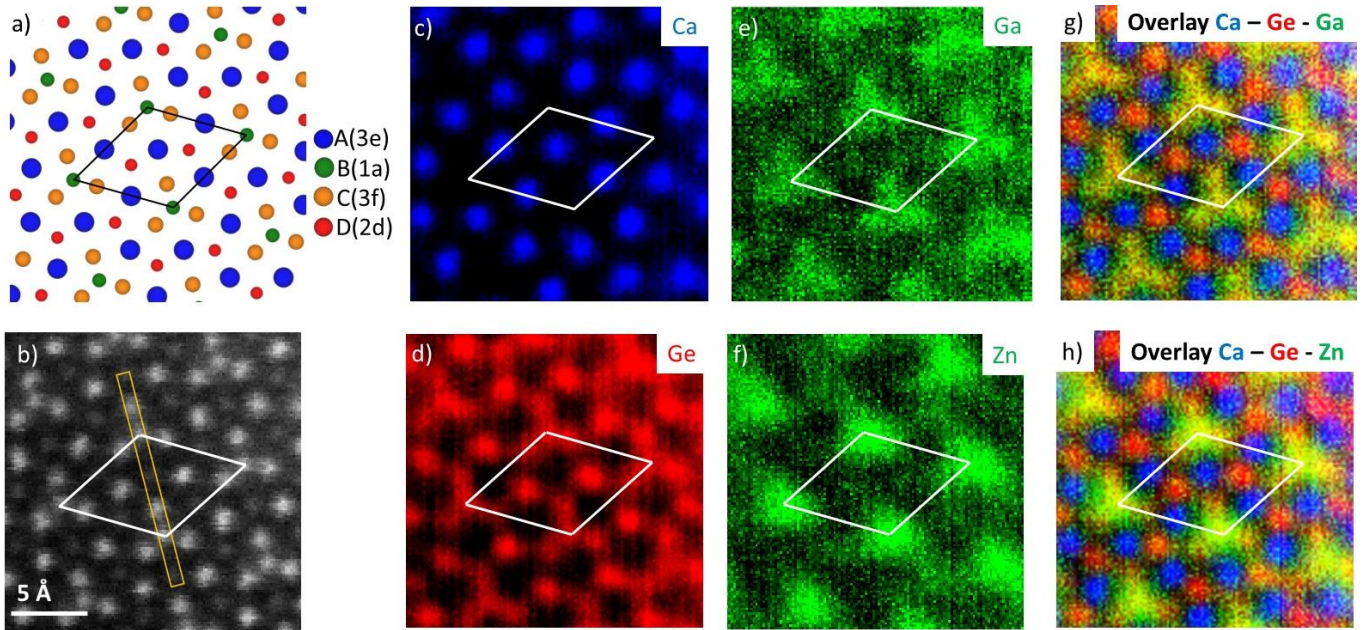


Figure 6. a) Scheme of the trigonal $P321$ structure projected along $[001]$, b) its corresponding atomic resolution STEM-HAADF image for the $\text{Ca}_3\text{GaZn}_{0.5}\text{Ge}_{4.5}\text{O}_{14}$ ($x=0.5$) composition. Atomic-scale STEM-EDS maps of the cations c) Ca in blue, d) Ge in red, e) Ga in green (Wiener filtered image) and f) Zn in green (Wiener strong filtered image). The overlaid EDS maps of “Ca, Ga, Ge” and “Ca, Zn, Ge” are shown in g) and h) respectively. The crystallographic unit cell is outlined in white in panels (b) – (h). The orange rectangle overlaid on (b) is the region used for 1D profile fitting presented in Figure 7.

The Ga and Ge signals appear clearly on both the 1a and 3f sites, while the Zn signal seems to be focused on the 1a sites; visually, it is difficult to confirm its presence on the 3f site. In order to gain more information and determine the Ga, Ge and Zn cation ratio on the 1a and 3f sites, a 1D analysis was performed by extracting an intensity profile through the sites from the EDS maps. The width of the profile (the orange rectangle overlaid on Figure 6b) was optimized in order to integrate as much signal as possible without introducing interference from the neighbouring 1a and 3f column signals. In such a configuration, with a small distance between the cation sites 1a – 3f ($\approx 1.9 \text{ \AA}$), it is not possible to integrate the full signal for each crystallographic site (Figure 6b).

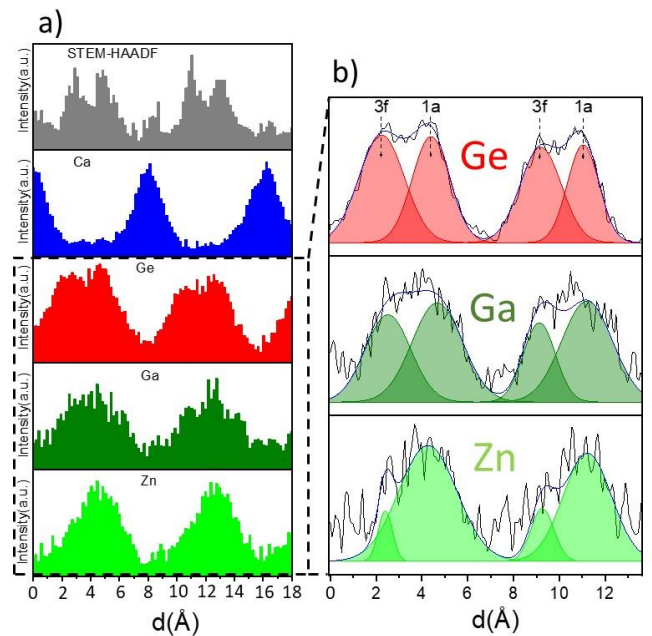


Figure 7. a) STEM-HAADF intensity profile in grey and EDS profiles of Ca, Ge, Ga and Zn (in blue, red, dark green and light green respectively). The signal was integrated from the drawn orange rectangle in Figure 6b. b) In black, EDS profiles of Ge, Ga and Zn extracted from the STEM-EDS raw maps. The signals are integrated through the orange strip on two neighbouring 1a and 3f sites (Figure 6b). The

calculated signals decomposed in Gaussian curves (blue), and the integrated areas (red for Ge, dark and light green for Ga and Zn respectively) under the calculated curves have been overlaid.

Using a Gaussian decomposition and assuming that the area under the curve is proportional to the element content, the ratios of the elements Ge, Ga and Zn between sites 1a and 3f were determined. The Gaussian coordinates were defined for the 1a and 3f sites from the Ge profile, which is best defined thanks to its high concentration, and then fixed for all the other element profiles (Ga and Zn) in order to integrate the signal in the same positions. As the Zn content is low, its profile was first refined using only one Gaussian contribution at the 1a coordinates (see Figure S14). However, a single Gaussian could not describe the entire profile, and a second Gaussian was added at the 3f position, indicating a small amount of Zn also present on this site. The calculated ratios between the 1a and 3f sites for the three cations were: ($\text{Ge}_{1a}/\text{Ge}_{3f} = 0.9$) ($\text{Ga}_{1a}/\text{Ga}_{3f} = 1.17$) ($\text{Zn}_{1a}/\text{Zn}_{3f} = 2.6$). Considering the nominal composition $\text{Ca}_3\text{GaZn}_{0.5}\text{Ge}_{4.5}\text{O}_{14}$, which has been checked by EDS analyses, and a 2d pure Ge site, the compositions of the mixed 1a and 3f sites have been determined and reported in Table 6: $0.23(10)\text{Zn} / 0.54(5)\text{Ge} / 0.28(8)\text{Ga}$ and $0.09(4)\text{Zn} / 0.67(2)\text{Ge} / 0.24(3)\text{Ga}$ respectively. These results show a very good agreement with refined occupancies from NPD data. Nevertheless, this 1D approach has certain limitations such as the application of a Wiener filter on the elementary maps, which can induce a bias, as well as the inability to integrate the signal through the entire sites due to the small distance between the

neighbouring 1a and 3f sites. Such problems can be reduced by a two-dimensional fitting approach such as that demonstrated by P. Lu *et al.*^{19,20} so that a wider region of the map is used for quantitative analysis.

We chose to analyse two regions from the central part of the 2D elemental images to minimize possible errors or deformation at the borders. These two regions are centered on 1a sites and extending to their first 3f and 2d neighbours, defining polygonal regions with minimal contributions of other sites (see Figure S15). We then performed a refinement for each cation (Zn, Ga and Ge) using the simplest possible model of a background offset and a sum of two-dimensional gaussian lines for each site. Each 2D gaussian is characterized by its x and y positions, width at half maximum, and amplitude.

The Ge data (with the best signal to noise ratio due to the high concentration of Ge in the cell) were refined first to extract the peak positions, width and amplitude for each of the 1a and 3f sites (note that the three 3f sites surrounding the 1a sites were constrained to keep the same peak width, for each of the two selected zones independently). The Zn and Ga data were then refined with constrained peak position and peak width from the Ge ones, hence extracting only the amplitude as refined value for these two cations on the 1a and 3f sites. Refinements of the STEM-EDS maps from zone 1 are shown in Figure 8. The equivalent zone 2 refinements are shown in Figure S16. The compositions of each column were extracted using the same calculation logic as the one used for the 1D refinements and normalizing the occupancies to 1.

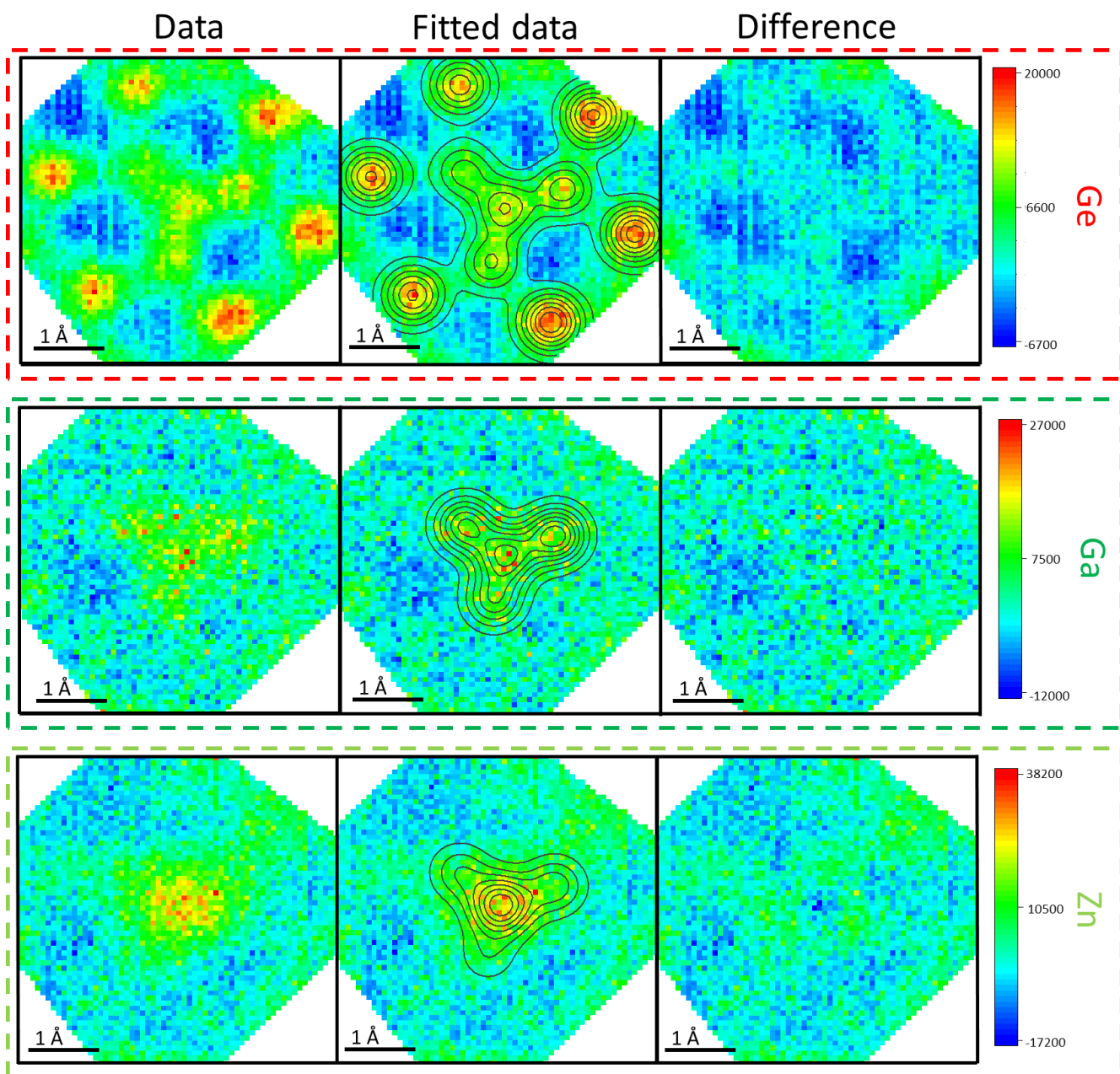


Figure 8. STEM-EDS 2D refinement plots of Ge, Ga and Zn from zone1, where the left column represents the data (after processing), the middle column fitted data (fit in black contours) and the difference plots in the right column.

Following the quantitative analysis by STEM-EDS, we constructed a Rietveld model for refinement against NPD data. Using the observation that the 2d site is dominated by Ge (Figure 6d and Figure 8), and by analogy with the $x = 0$ and 1 members (Tables 1 and 2), we fixed the 2d site in $x = 0.5$ to be occupied exclusively by Ge. We then populated the 1a and 3f sites with the remaining Zn, Ga and Ge atoms, weighted according to their apparent site preferences from STEM-EDS and end-member Rietveld refinements ($0.25\text{Ga}/0.251\text{Zn}/0.5\text{Ge}$ and $0.25\text{Ga}/0.083\text{Zn}/0.667\text{Ge}$ for the 1a and 3f respectively). Constraints were then applied to (i) keep each site fully occupied by cations ($\text{Zn} + \text{Ga} + \text{Ge} = 1$) and (ii) fix the global composition to the nominal value

$\text{Ca}_3\text{GaGe}_{4.5}\text{Zn}_{0.5}\text{O}_{14}$. The Zn, Ga and Ge occupancies of 1a and 3f were then refined subject to these constraints.

The refined Zn and Ge occupancies on both sites led to a Zn distribution close to the one in the $\text{Ca}_3\text{ZnGe}_5\text{O}_{14}$ $x=1$ compound where Zn and Ga are disposed in a 43(6)%/57(6)% and 25(2)%/75(2)% ratios between the two 1a and 3f sites respectively, while Ge is disposed between the 1a, 3f and 2d sites in a 0.12(1)%/0.44(1)%/0.44% ratio, see Figure 9 and Table 5 for refined plot and parameters. The results show a good agreement between the Rietveld refinement and the STEM-EDS results, as shown in Table 6.

Table 5. Refined structural parameters obtained from NPD data collected at room temperature on $\text{Ca}_3\text{GaZn}_{0.5}\text{Ge}_{4.5}\text{O}_{14}$ ($x=0.5$) ($P321$ space group, $a= 8.0460(2)$ Å and $c= 4.9994(2)$ Å) sample.

Atom	Position	x	y	z	Occupancy	B_{iso}
Ca	3e	0.4198(7)	0	0	1	1.12(11)
Ga1/Ge1/Zn1	1a	0	0	0	0.25(2)/0.531(15)/0.22(3)	0.98(6) ^a
Ga2/Ge2/Zn2	3f	0.7648(4)	0	1/2	0.250(8)/0.656(5)/0.094(10)	0.98(6) ^a
Ge3	2d	1/3	2/3	0.5283(9)	1	0.98(6) ^a
O1	2d	1/3	2/3	0.1874(13)	1	1.66(5) ^b
O2	6g	0.4629(5)	0.3175(4)	0.3120(7)	1	1.66(5) ^b
O3	6g	0.2208(5)	0.0788(4)	0.7631(7)	1	1.66(5) ^b

^{a,b}: constrained to refine to the same B_{iso} values.

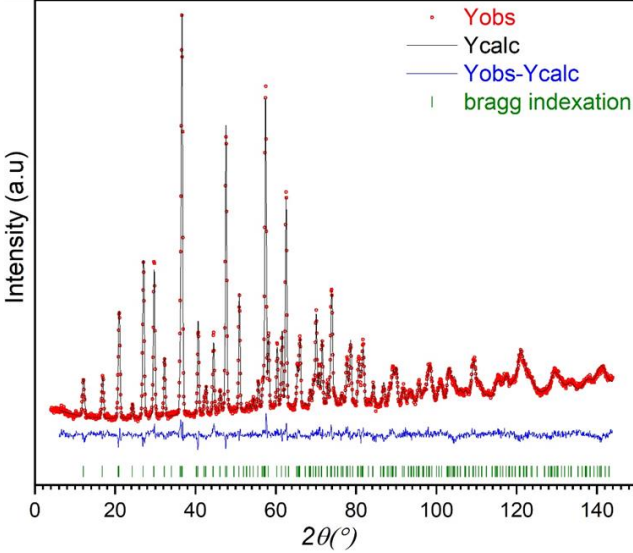


Figure 9. NPD Rietveld refinements plot of $\text{Ca}_3\text{GaZn}_{0.5}\text{Ge}_{4.5}\text{O}_{14}$ ($x=0.5$) $R_p= 2.97\%$ $R_{wp}= 3.80\%$. Observed (red dot), calculated (black line), and difference (blue line) profiles are shown. The green tick marks correspond to allowed reflection positions.

Table 6. Refined occupancies for Zn, Ga and Ge on the 1a, 3f and 2d sites, extracted from NPD data and STEM-EDS maps.

		Site	1a	3f	2d
		Atom			
NPD Refinement	Zn		0.22(3)	0.09(1)	0
	Ga		0.25(2)	0.25(1)	0
	Ge		0.53(2)	0.66(1)	1
1D Refinement	Zn		0.23(10) ^a	0.09(4) ^a	0
	Ga		0.28(8) ^a	0.24(3) ^a	0
	Ge		0.54(5) ^a	0.67(2) ^a	1
2D Refinement	Zn		0.18(3) ^b	0.11(3) ^b	0
	Ga		0.24(2) ^b	0.26(2) ^b	0
	Ge		0.59(2) ^b	0.64(2) ^b	1

^a Errors were estimated by calculating standard deviation from the fitted areas of the 1D EDS profiles over the averaged 4 (1a, 3f sites) on the cell corners, shown in figure 6e, 6d and 6f.

^b Mean values from zone1 and zone2 refinements. See Table S11 for zone1 and zone2 individual refined occupancies.

4. Discussion

High-resolution SPD shows that the crystal structures of $\text{Ca}_3\text{Ga}_{2-2x}\text{Ge}_{4+x}\text{Zn}_x\text{O}_{14}$ ($0 \leq x \leq 1$) can all be indexed to a trigonal unit cell ($P321$) when crystallized from precursor glasses or directly from their melts. This is consistent with the reported crystal structure of $\text{Ca}_3\text{Ga}_2\text{Ge}_4\text{O}_{14}$, which is also trigonal when synthesized by single crystal growth methods, but it contrasts with a previous study on $\text{Ca}_3\text{ZnGe}_5\text{O}_{14}$ single crystals which are metrically monoclinic. As described in section 3.2, the refinement of trigonal and monoclinic models against the acquired SPD pattern of $\text{Ca}_3\text{ZnGe}_5\text{O}_{14}$ ($x=1$) produced very similar fits and near-identical structures, and we thus retained the simpler trigonal model as the most appropriate structural description. The underlying difference between trigonal glass-crystallized $\text{Ca}_3\text{ZnGe}_5\text{O}_{14}$ and monoclinic single-crystal $\text{Ca}_3\text{ZnGe}_5\text{O}_{14}$ ¹⁴ lies in the distribution of Zn^{2+} and Ge^{4+} between the octahedral (1a) and tetrahedral (3f) sites. In single-crystal $\text{Ca}_3\text{ZnGe}_5\text{O}_{14}$,¹⁴ these cations are fully ordered with Zn^{2+} exclusively in octahedral coordination. In contrast, glass-crystallized $\text{Ca}_3\text{ZnGe}_5\text{O}_{14}$ contains a significant amount of site inversion with Zn^{2+} partially occupying the tetrahedral 3f sites. This can also be seen by comparison of the B-C- and D-site polyhedral volumes of the two structures. In Table 7, we show a comparison between the octahedral (1a), tetrahedral (3f and 2d) Zn-O distances in glass-crystallized (trigonal) and single crystal (monoclinic) $\text{Ca}_3\text{ZnGe}_5\text{O}_{14}$: in the trigonal structure, these distances are significantly shorter for the 1a site, and slightly longer for the 3f, while they show similar values for the 2d site, consistent with refined partial occupancies of only the 1a and 3f by smaller Ge^{4+} and bigger Zn^{2+} . We note that the symmetry-reducing monoclinic distortion is not a prerequisite for this type of $\text{Zn}^{2+}/\text{Ge}^{4+}$ ordering, which implies that the monoclinic distortion of the lattice is induced by the cation ordering and its associated changes in the average size of the framework polyhedra.

Table 7. Comparison between the reported C2¹⁴ and NPD refined P321 M-O bond of the Ca₃ZnGe₅O₁₄ (x=1) composition.

		Reported C2	Refined P321
Bond lengths (Å)	M1-O1* x2	2.10(1)	1.985(2)
	M1-O4* x2	2.008(9)	1.985(2)
	M1-O6* x2	1.992(8)	1.985(2)
V (Å ³)	M1* octa site	10.77(2)	10.08(2)
Bond lengths (Å)	M1-O6* x1	1.731(8)	1.740(1)
	M1-O2* x1	1.830(7)	1.862(6)
	M1-O1* x1	1.718(10)	1.740(1)
	M1-O7* x1	1.830(7)	1.862(6)
V (Å ³)	M1* tetra site	2.74(2)	2.86(2)
Bond lengths (Å)	M3-O4* x2	1.749(9)	1.862(6)
	M3-O3* x2	1.852(7)	1.767(6)
V (Å ³)	M3* tetra site	2.77(2)	2.86(2)
Bond lengths (Å)	M2-O7* x1	1.768(6)	1.770(7)
	M2-O5* x1	1.714(8)	1.727(11)
	M2-O3* x1	1.767(7)	1.770(7)
	M2-O2* x1	1.769(7)	1.770(7)
V (Å ³)	M2* tetra site	2.71(2)	2.74(2)

*M-O atoms notation taken from C2 model, see Table S10 for the P321 analogue atoms

At the other extreme of the solid solution, Ca₃Ga₂Ge₄O₁₄ (x = 0), there are some minor differences in the extent of Ga³⁺/Ge⁴⁺ ordering between the melt-crystallized materials that we report here, and single-crystal materials described in the literature,³³ despite the retention of trigonal P321 symmetry (see Table 8). In melt-crystallized Ca₃Ga₂Ge₄O₁₄, Ga³⁺ ions are distributed over the octahedral 1a and tetrahedral 3f sites, while the tetrahedral 2d sites are occupied exclusively by Ge⁴⁺; only 25(4)% of the total Ga content is in octahedral coordination, whereas the remaining 75(4)% is tetrahedrally coordinated. This is consistent with the reported Ga/Ge coordination environments in Ca₃Ga₂Ge₄O₁₄ glass determined by EXAFS.³⁴ In single-crystal Ca₃Ga₂Ge₄O₁₄,³³ anomalous X-ray scattering methods have shown that only ~10% of the Ga³⁺ cations are present in octahedral coordination (1a), with the remainder present at the tetrahedral (3f) site. In both materials, the tetrahedral 2d site is occupied exclusively by Ge⁴⁺, which may help to maximize separation of the most highly charged cations, and hence minimize electrostatic repulsion between them. This confirms that the synthesis route can influence the extent of Ga³⁺/Ge⁴⁺ ordering in these structures, with melt-crystallization favouring a higher degree of disorder in this case, compared to the single crystals synthesized by a Czochralski method.³³

Table 8. Comparison between the refined occupancies of Ga and Ge in the 1a, 3f and 2d sites from melt-crystallized (this work) and single crystal³³ on the Ca₃Ga₂Ge₄O₁₄ (x=0) compound.

Site \ Atom	Melt-crystallized			Single crystal ³³		
	1a	3f	2d	1a	3f	2d
Ga	0.51(8)	0.50(3)	0	0.2	0.6	0
Ge	0.49(8)	0.50(3)	1	0.8	0.4	1

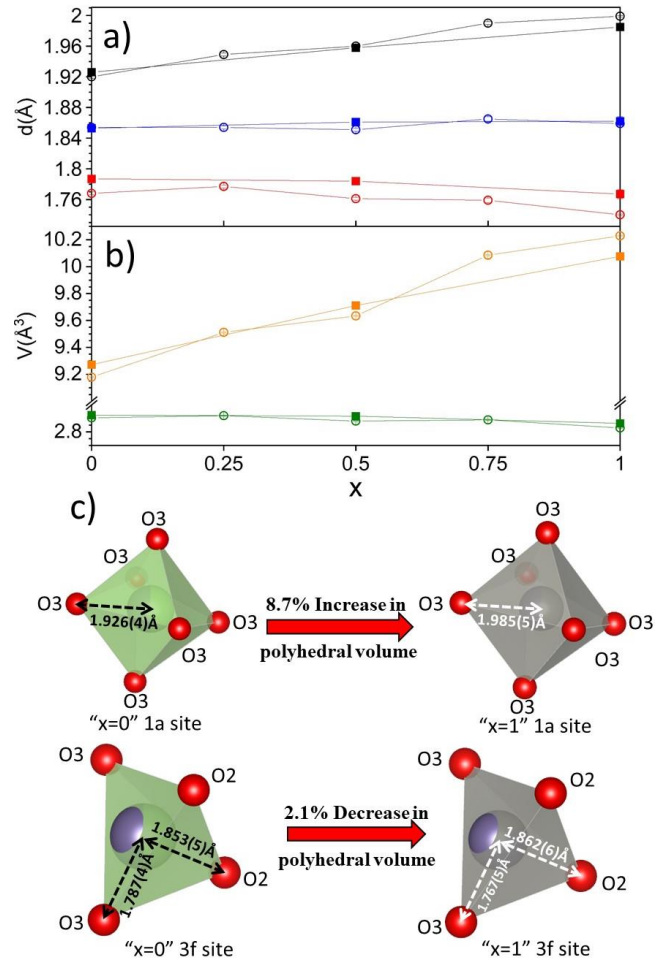


Figure 10. Refined M-O distances from SPD and NPD (hollow circles and filled squares respectively) for compositions 0 ≤ x ≤ 1. (a) B-O3 (black), C-O2 (blue) and C-O3 (red) distances, and (b) their corresponding polyhedral volumes BO₆ (1a, orange) and CO₄ (3f, green). (c) Cationic 1a and 3f site coordination and their nearby interatomic distances for both x=0 and x=1 compounds from NPD refinements.

In complex glass-crystallized compositions with three isoelectronic cations (Zn²⁺/Ga³⁺/Ge⁴⁺) distributed over the three possible octahedral and tetrahedral framework sites, exemplified by Ca₃GaZn_{0.5}Ge_{4.5}O₁₄ (x = 0.5) which is reported here for the first time, a combined approach between NPD refinements and quantitative 2D fitting to atomic resolution STEM-EDS maps was applied. The analysis of Ca₃GaZn_{0.5}Ge_{4.5}O₁₄ shows that the structure evolves progressively as the solid solution is traversed. This is seen in the unit cell parameters

(Figure 3c) and the Rietveld refined M-O distances at the 1a (octahedral), 3f (tetrahedral) and 2d (tetrahedral) framework sites (Figure 10): as Zn^{2+} is substituted into the structure, there is a marked increase in the volume of the MO_6 octahedra which goes against the overall decreasing trend in unit cell volume, indicating that the 1a site is becoming preferentially populated by larger cations. It was possible to quantify directly the cation distribution in $\text{Ca}_3\text{GaZn}_{0.5}\text{Ge}_{4.5}\text{O}_{14}$ ($x = 0.5$) by 2D fitting to atomic resolution STEM-EDS images followed by NPD refinements: this confirmed directly that Zn^{2+} shows the strongest preference for octahedral coordination, whilst Ga^{3+} and Ge^{4+} have similar proportions in octahedral and tetrahedral coordination (and that, in common with the end member compositions, the 2d tetrahedral site is occupied exclusively by Ge^{4+}). This distribution is essentially consistent with the relative ionic radii of these cations. Across the solid solution, there is also a notable increase of the refined oxygen thermal parameter values, from $B_{\text{iso}} = 1.18(4)\text{\AA}^2$ ($x=0$), $1.66(5)\text{\AA}^2$ ($x=0.5$) to $2.17(7)\text{\AA}^2$ ($x=1$), consistent with the observed cationic disorder and the increase of the size mismatch at the B and C sites due to the Ga^{3+} substitution by Zn^{2+} and Ge^{4+} .

Characterization of the cation distributions in complex bulk materials containing several cations with close atomic and neutron scattering factors is a non-trivial problem that is usually approached by coupling different characterization techniques. For example, a recent study of the high entropy spinel $(\text{Cr}_{0.2}\text{Mn}_{0.2}\text{Fe}_{0.2}\text{Co}_{0.2}\text{Ni}_{0.2})_3\text{O}_4$ with five different first-row transition metal cations distributed over two crystallographic sites, combines multiple complementary diffraction and spectroscopic techniques to fully characterize the material.³⁵ Our analysis of the $\text{Zn}^{2+}/\text{Ga}^{3+}/\text{Ge}^{4+}$ distribution over three crystallographic sites in $\text{Ca}_3\text{GaZn}_{0.5}\text{Ge}_{4.5}\text{O}_{14}$ demonstrates that the quantitative use of atomic resolution STEM-EDS mapping, using a 2D fitting programme to directly extract the occupancies of each element, has the potential to be very useful for such problems that can simplify crystallographic analysis and can be applied in many different contexts if sufficiently high-quality data can be obtained from a suitable crystallite orientation. Here, we have shown that it is possible to fit the different elemental contributions from atomic columns with extremely small spatial separations (e.g. atomic columns spaced by approximately 2\AA are clearly resolved in the case of Ge^{4+} , as shown in Figure 6) and with relatively low cation concentrations (e.g. a Zn^{2+} 3f site occupancy of 0.1). For Zn^{2+} and Ga^{3+} , which have weaker STEM-EDS signals due to their low populations in $\text{Ca}_3\text{GaZn}_{0.5}\text{Ge}_{4.5}\text{O}_{14}$, 2D fitting makes it possible to extract independent occupancies from the adjacent 1a and 3f sites. Such high spatial resolution and sensitivity should make it possible to study many different structure types in this way.

5. Conclusion

We have synthesized a new solid solution $\text{Ca}_3\text{Ga}_{2-2x}\text{Zn}_x\text{Ge}_{4+x}\text{O}_{14}$ ($0 \leq x \leq 1$) by direct crystallization from an under-cooled melt ($x = 0$) and glass crystallization ($0.25 \leq x \leq 1$), and characterized the evolution of structure and cation distribution across the solid solution by coupling SPD and NPD to atomic resolution STEM-EDS. We showed that the trigonal langasite structure (space group $P321$) can be retained across the whole solid solution, even for the composition $\text{Ca}_3\text{ZnGe}_5\text{O}_{14}$ ($x = 1$), which was previously reported in a distorted monoclinic langasite structure (space group $C2$). Using NPD, we found that the simpler end-member compounds $\text{Ca}_3\text{Ga}_2\text{Ge}_4\text{O}_{14}$ ($x = 0$) and $\text{Ca}_3\text{ZnGe}_5\text{O}_{14}$ ($x = 1$) have isoelectronic cations (respectively $\text{Ga}^{3+}/\text{Ge}^{4+}$ and $\text{Zn}^{2+}/\text{Ge}^{4+}$) distributed over the tetrahedral 3f and octahedral 1a sites, while the tetrahedral 2d sites are occupied exclusively by Ge^{4+} . This partial disordering of Zn^{2+} and Ge^{4+} over two crystallographic sites in glass-crystallized $\text{Ca}_3\text{ZnGe}_5\text{O}_{14}$ marks a major difference from its previously reported monoclinic structure, which is fully-ordered with Zn^{2+} in purely octahedral coordination (1a) and Ge^{4+} purely tetrahedral (3f). The partial disordering of $\text{Zn}^{2+}/\text{Ge}^{4+}$, introduced by the crystallization from glass synthesis technique, presumably accounts for the suppression of the monoclinic distortion and stabilization of the trigonal structure in this material.

In the more complex case of $\text{Ca}_3\text{GaZn}_{0.5}\text{Ge}_{4.5}\text{O}_{14}$ ($x=0.5$), where three isoelectronic cations (Zn^{2+} , Ga^{3+} and Ge^{4+}) can be distributed over three possible sites, we used atomic-resolution STEM-EDS to image their distributions directly, and then extracted their site occupancy values quantitatively via 2D fitting by adapting the Fit2D programme (developed originally for fitting 2D NMR spectra). This allowed us to construct a suitable Rietveld model for refinement against NPD data using chemically justified site occupancy constraints. These results confirmed that the tetrahedral 2d site is occupied exclusively by Ge^{4+} at $x = 0.5$ (in common with the simpler $x = 0, 1$ end members), whilst Zn^{2+} , Ga^{3+} and the remaining Ge^{4+} are distributed over the octahedral (1a) and tetrahedral (3f) sites in proportions that correlate to their ionic radii: the Zn^{2+} ions show the greatest tendency towards octahedral coordination, whilst a higher proportion of Ga^{3+} and Ge^{4+} are present at the 3f sites. To our knowledge, this is the first time that quantitative 2D fitting of atomic resolution STEM-EDS maps has been applied to this type of problem in a bulk oxide material. In principle, this approach can be applied to other materials classes where it is important to understand the distributions of cations with similar scattering factors (e.g. adjacent transition metals, lanthanides or p -block elements) over multiple crystallographic sites within a structure.

6. Associated Content

The used code for 2D refinements of STEM-EDS maps and refined data are available at:

<https://github.com/DoMassiot/Fit2DLangasiteData>

Supporting Information

The Supporting Information is available free of charge at:

(Website)

Solid state synthesis description, ^{71}Ga NMR, VT-PXRD, Rietveld refined SDP data plots, STEM-EDS refined zones, Rietveld refined structural parameters.

Accession Codes

CCDC 2163439-2163441 contain the supplementary crystallographic data for this paper. These data can be obtained free of charge via www.ccdc.cam.ac.uk/data_request/cif, or by emailing data_request@ccdc.cam.ac.uk, or by contacting The Cambridge Crystallographic Data Centre, 12 Union Road, Cambridge CB2 1EZ, UK; fax: +44 1223 336033.

7. Acknowledgements

This work was supported by the Agence Nationale de la Recherche (France), under the project PERSIST (ANR-18-CE08-0012), and has also benefited from the electron microscopy facilities of the Platform MACLE-CVL, which was co-funded by the European Union and Centre-Val de Loire Region (FEDER). We thank Sandra Ory (CEMHTI, Orléans, France) for assistance with DSC measurements. Neutron diffraction experiments were carried out by Charles Hervoche at the CANAM infrastructure of the Nuclear Physics Institute (Řež, Czech Republic) and infrastructure of reactors LVR-15 and LR-0, supported through the Ministry of Education, Youth and Sports project LM2015056 and LM2018120, respectively. Use of the Advanced Photon Source at Argonne National Laboratory was supported by the U. S. Department of Energy, Office of Science, Office of Basic Energy Sciences, under Contract No. DE-AC02-06CH11357.

8. References

- (1) Boyer, M.; Carrion, A. J. F.; Ory, S.; Becerro, A. I.; Villette, S.; Eliseeva, S. V.; Petoud, S.; Aballea, P.; Matzen, G.; Allix, M. Transparent Polycrystalline $\text{SrREGa}_3\text{O}_7$ Melilite Ceramics: Potential Phosphors for Tuneable Solid State Lighting. *J. Mater. Chem. C* **2016**, *4* (15), 3238–3247. <https://doi.org/10.1039/C6TC00633G>.
- (2) Boyer, M.; Alahraché, S.; Genevois, C.; Licheron, M.; Lefevre, F.-X.; Castro, C.; Bonnefont, G.; Patton, G.; Moretti, F.; Dujardin, C.; Matzen, G.; Allix, M. Enhanced Transparency through Second Phase Crystallization in BaAl_4O_7 Scintillating Ceramics. *Cryst. Growth Des.* **2016**, *16* (1), 386–395. <https://doi.org/10.1021/acs.cgd.5b01374>.
- (3) Allix, M.; Alahrache, S.; Fayon, F.; Suchomel, M.; Porcher, F.; Cardinal, T.; Matzen, G. Highly Transparent BaAl_4O_7 Polycrystalline Ceramic Obtained by Full Crystallization from Glass. *Adv. Mater.* **2012**, *24* (41), 5570–5575. <https://doi.org/10.1002/adma.201202282>.
- (4) Fernandez-Carrion, A. J.; Al Saghir, K.; Veron, E.; Becerro, A. I.; Porcher, F.; Wisniewski, W.; Matzen, G.; Fayon, F.; Allix, M. Local Disorder and Tunable Luminescence in $\text{Sr}_{1-x/2}\text{Al}_{2-x}\text{Si}_x\text{O}_4$ ($0.2 \leq x \leq 0.5$) Transparent Ceramics. *Inorg. Chem.* **2017**, *56* (23), 14446–14458. <https://doi.org/10.1021/acs.inorgchem.7b01881>.
- (5) Irifune, T.; Kawakami, K.; Arimoto, T.; Ohfuji, H.; Kunimoto, T.; Shinmei, T. Pressure-Induced Nano-Crystallization of Silicate Garnets from Glass. *Nat. Commun.* **2016**, *7* (1), 13753. <https://doi.org/10.1038/ncomms13753>.
- (6) Ma, X.; Li, X.; Li, J.; Genevois, C.; Ma, B.; Etienne, A.; Wan, C.; Véron, E.; Peng, Z.; Allix, M. Pressureless Glass Crystallization of Transparent Yttrium Aluminum Garnet-Based Nanoceramics. *Nat. Commun.* **2018**, *9* (1), 1175. <https://doi.org/10.1038/s41467-018-03467-7>.
- (7) Bertrand, A.; Carraud, J.; Chenu, S.; Allix, M.; Véron, E.; Duclère, J.; Launay, Y.; Hayakawa, T.; Genevois, C.; Brisset, F.; Célarié, F.; Thomas, P.; Delaizir, G. Scalable and Formable Tellurite-Based Transparent Ceramics for Near Infrared Applications. *Adv. Opt. Mater.* **2016**, *4* (10), 1482–1486. <https://doi.org/10.1002/adom.201600230>.
- (8) Al Saghir, K.; Chenu, S.; Veron, E.; Fayon, F.; Suchomel, M.; Genevois, C.; Porcher, F.; Matzen, G.; Massiot, D.; Allix, M. Transparency through Structural Disorder: A New Concept for Innovative Transparent Ceramics. *Chem. Mater.* **2015**, *27* (2), 508–514. <https://doi.org/10.1021/cm5037106>.
- (9) Allix, M.; Chenu, S.; Véron, E.; Poumeyrol, T.; Kouadri-Boudjelthia, E. A.; Alahraché, S.; Porcher, F.; Massiot, D.; Fayon, F. Considerable Improvement of Long-Persistent Luminescence in Germanium and Tin Substituted ZnGa_2O_4 . *Chem. Mater.* **2013**, *25*

- (9), 1600–1606.
<https://doi.org/10.1021/cm304101n>.
- (10) Chenu, S.; Véron, E.; Genevois, C.; Matzen, G.; Cardinal, T.; Etienne, A.; Massiot, D.; Allix, M. Tuneable Nanostructuring of Highly Transparent Zinc Gallogermanate Glasses and Glass-Ceramics. *Adv. Opt. Mater.* **2014**, *2* (4), 364–372.
<https://doi.org/10.1002/adom.201400007>.
- (11) Chenu, S.; Véron, E.; Genevois, C.; Garcia, A.; Matzen, G.; Allix, M. Long-Lasting Luminescent $\text{ZnGa}_2\text{O}_4:\text{Cr}^{3+}$ Transparent Glass-Ceramics. *J Mater Chem C* **2014**, *2* (46), 10002–10010.
<https://doi.org/10.1039/C4TC02081B>.
- (12) Zhang, S.; Yu, F. Piezoelectric Materials for High Temperature Sensors. *J. Am. Ceram. Soc.* **2011**, *94* (10), 3153–3170.
<https://doi.org/10.1111/j.1551-2916.2011.04792.x>.
- (13) Diaz-Lopez, M.; Shin, J. F.; Li, M.; Dyer, M. S.; Pitcher, M. J.; Claridge, J. B.; Blanc, F.; Rosseinsky, M. J. Interstitial Oxide Ion Conductivity in the Langasite Structure: Carrier Trapping by Formation of $(\text{Ga,Ge})_2\text{O}_8$ Units in $\text{La}_{28}\text{Ga}_{5-x}\text{Ge}_{1+x}\text{O}_{14+x/2}$ ($0 < x \leq 1.5$). *Chem. Mater.* **2019**, *31* (15), 5742–5758.
<https://doi.org/10.1021/acs.chemmater.9b01734>.
- (14) Redhammer, G. J. $\text{Ca}_3\text{ZnGeO}_2[\text{Ge}_4\text{O}_{12}]$: A Ca–Zn Germanate Related to the Mineral Taikanite. *Acta Crystallogr. Sect. C Struct. Chem.* **2015**, *71* (1), 80–83.
<https://doi.org/10.1107/S2053229614027466>.
- (15) Pavlovskaya, A.; Werner, S.; Maximov, B.; Mill, B. Pressure-Induced Phase Transitions of Piezoelectric Single Crystals from the Langasite Family: $\text{La}_3\text{Nb}_{0.5}\text{Ga}_{5.5}\text{O}_{14}$ and $\text{La}_3\text{Ta}_{0.5}\text{Ga}_{5.5}\text{O}_{14}$. *Acta Crystallogr. B* **2002**, *58* (6), 939–947.
<https://doi.org/10.1107/S0108768102010273>.
- (16) Mill, B. V.; Maksimov, B. A.; Pisarevskii, Yu. V.; Danilova, N. P.; Pavlovskaya, A.; Werner, S.; Schneider, J. Phase Transitions in Compounds with the $\text{Ca}_3\text{Ga}_2\text{Ge}_4\text{O}_{14}$ Structure. *Crystallogr. Rep.* **2004**, *49* (1), 60–69.
<https://doi.org/10.1134/1.1643965>.
- (17) Mill, B. V.; Klimenkova, A. A.; Maximov, B. A.; Molchanov, V. N.; Pushcharovsky, D. Yu. Enantiomorphism of the $\text{Ca}_3\text{Ga}_2\text{Ge}_4\text{O}_{14}$ Compound and Comparison of the $\text{Ca}_3\text{Ga}_2\text{Ge}_4\text{O}_{14}$ and $\text{Sr}_3\text{Ga}_2\text{Ge}_4\text{O}_{14}$ Structures. *Crystallogr. Rep.* **2007**, *52* (5), 785–794.
<https://doi.org/10.1134/S1063774507050069>.
- (18) Lu, P.; Xiong, J.; Van Benthem, M.; Jia, Q. Atomic-Scale Chemical Quantification of Oxide Interfaces Using Energy-Dispersive X-Ray Spectroscopy. *Appl. Phys. Lett.* **2013**, *102* (17), 173111.
<https://doi.org/10.1063/1.4804184>.
- (19) Lu, P.; Romero, E.; Lee, S.; MacManus-Driscoll, J. L.; Jia, Q. Chemical Quantification of Atomic-Scale EDS Maps under Thin Specimen Conditions. *Microsc. Microanal.* **2014**, *20* (6), 1782–1790.
<https://doi.org/10.1017/S1431927614013245>.
- (20) Lu, P.; Zhou, L.; Kramer, M. J.; Smith, D. J. Atomic-Scale Chemical Imaging and Quantification of Metallic Alloy Structures by Energy-Dispersive X-Ray Spectroscopy. *Sci. Rep.* **2014**, *4* (1), 3945.
<https://doi.org/10.1038/srep03945>.
- (21) Niu, H. J.; Pitcher, M. J.; Corkett, A. J.; Ling, S.; Mandal, P.; Zanella, M.; Dawson, K.; Stamenov, P.; Batuk, D.; Abakumov, A. M.; Bull, C. L.; Smith, R. I.; Murray, C. A.; Day, S. J.; Slater, B.; Cora, F.; Claridge, J. B.; Rosseinsky, M. J. Room Temperature Magnetically Ordered Polar Corundum GaFeO_3 Displaying Magnetoelectric Coupling. *J. Am. Chem. Soc.* **2011**, *133* (1), 33–35.
- (22) Roychowdhury, S.; Ghosh, T.; Arora, R.; Samanta, M.; Xie, L.; Singh, N. K.; Soni, A.; He, J.; Waghmare, U. V.; Biswas, K. Enhanced Atomic Ordering Leads to High Thermoelectric Performance in AgSbTe_2 . *Science* **2021**, *371* (6530), 722–727.
<https://doi.org/10.1126/science.abb3517>.
- (23) Mohanty, D.; Sefat, A. S.; Li, J.; Meisner, R. A.; Rondinone, A. J.; Payzant, E. A.; Abraham, D. P.; Wood III, D. L.; Daniel, C. Correlating Cation Ordering and Voltage Fade in a Lithium–Manganese-Rich Lithium-Ion Battery Cathode Oxide: A Joint Magnetic Susceptibility and TEM Study. *Phys. Chem. Chem. Phys.* **2013**, *15* (44), 19496.
<https://doi.org/10.1039/c3cp53658k>.
- (24) Rietveld, H. M. A Profile Refinement Method for Nuclear and Magnetic Structures. *J. Appl. Crystallogr.* **1969**, *2* (2), 65–71.
<https://doi.org/10.1107/S0021889869006558>.
- (25) Coelho, A. A. TOPAS and TOPAS-Academic: An Optimization Program Integrating Computer Algebra and Crystallographic Objects Written in C++. *J. Appl. Crystallogr.* **2018**, *51* (1), 210–218.
<https://doi.org/10.1107/S1600576718000183>.
- (26) Brown, I. D.; Altermatt, D. Bond-Valence Parameters Obtained from a Systematic Analysis of the Inorganic Crystal Structure Database. *Acta Crystallogr. B* **1985**, *41* (4), 244–247.
<https://doi.org/10.1107/S0108768185002063>.
- (27) Genevois, C.; Bazzaoui, H.; Boyer, M.; Ory, S.; Ledemi, Y.; Messaddeq, Y.; Pitcher, M. J.; Allix, M. Emergence of A-Site Cation Order in the Small Rare-Earth Melilites $\text{SrREGa}_3\text{O}_7$ (

RE = Dy–Lu, Y). *Inorg. Chem.* **2021**, *60* (16), 12339–12354.

<https://doi.org/10.1021/acs.inorgchem.1c01565>

- (28) Shannon, R. D. Revised Effective Ionic Radii and Systematic Studies of Interatomic Distances in Halides and Chalcogenides. *Acta Crystallogr. A* **1976**, *32* (5), 751–767.
- (29) Stephens, P. W. Phenomenological Model of Anisotropic Peak Broadening in Powder Diffraction. *J. Appl. Crystallogr.* **1999**, *32* (2), 281–289.
<https://doi.org/10.1107/S0021889898006001>.
- (30) Sears, V. F. Neutron Scattering Lengths and Cross Sections. *Neutron News* **1992**, *3* (3), 26–37.
<https://doi.org/10.1080/10448639208218770>.
- (31) Belokoneva, E. L.; Belov, N. V. Crystal Structure of Synthetic Ga,Ge-Helenite, $\text{Ca}_2\text{Ga}_2\text{GeO}_7 = \text{Ca}_2\text{Ga}(\text{GaGe})\text{O}_7$, and Its Comparison with the Structure of $\text{Ca}_3\text{Ga}_2\text{Ge}_4\text{O}_{14} = \text{Ca}_3\text{Ge}(\text{Ga}_2\text{Ge})\text{Ge}_2\text{O}_{14}$. In *Doklady Akademii Nauk*; Russian Academy of Sciences, 1981; Vol. 260, pp 1363–1366.
- (32) Stadelmann, P. JEMS <https://www.jems-swiss.ch/> (accessed 2022 -03 -01).
- (33) Dudka, A. P.; Mill', B. V. Accurate Crystal-Structure Refinement of $\text{Ca}_3\text{Ga}_2\text{Ge}_4\text{O}_{14}$ at 295 and 100K and Analysis of the Disorder in the Atomic Positions. *Crystallogr. Rep.* **2013**, *58* (4), 594–603.
<https://doi.org/10.1134/S1063774513040081>.
- (34) Chelstowski, D.; Witkowska, A.; Rybicki, J.; Padlyak, B.; Trapananti, A.; Principi, E. EXAFS Study of Glasses of the $\text{CaO-Ga}_2\text{O}_3\text{-GeO}_2$ System. *Opt. Appl.* **2003**, *33* (1), 125–132.
- (35) Sarkar, A.; Eggert, B.; Witte, R.; Lill, J.; Velasco, L.; Wang, Q.; Sonar, J.; Ollefs, K.; Bhattacharya, S. S.; Brand, R. A.; Wende, H.; de Groot, F. M. F.; Clemens, O.; Hahn, H.; Kruk, R. Comprehensive Investigation of Crystallographic, Spin-Electronic and Magnetic Structure of $(\text{Co}_{0.2}\text{Cr}_{0.2}\text{Fe}_{0.2}\text{Mn}_{0.2}\text{Ni}_{0.2})_3\text{O}_4$: Unraveling the Suppression of Configuration Entropy in High Entropy Oxides. *Acta Mater.* **2022**, *226*, 117581.
<https://doi.org/10.1016/j.actamat.2021.117581>.